


Article

Steam Reforming of Methanol over Nanostructured Pt/TiO₂ and Pt/CeO₂ Catalysts for Fuel Cell Applications

Joan Papavasiliou^{1,2,*}, Alexandra Paxinou^{1,2}, Grzegorz Słowik³, Stylianos Neophytides² and George Avgouropoulos^{1,*} ¹ Department of Materials Science, University of Patras, GR-26504 Patras, Greece; paxinou@upatras.gr² Foundation for Research and Technology-Hellas (FORTH), Institute of Chemical Engineering Sciences (ICE-HT), P.O. Box 1414, GR-26504 Patras, Greece; neoph@iceht.forth.gr³ Faculty of Chemistry, University of Maria Curie-Skłodowska, Pl. M. Curie-Skłodowskiej 2, 20-031 Lublin, Poland; grzegorz.slowik@poczta.umcs.lublin.pl

* Correspondence: jpapav@iceht.forth.gr (J.P.); geoavg@upatras.gr (G.A.); Tel.: +30-2610-965319 (J.P.); +30-2610-969811 (G.A.)

Received: 30 October 2018; Accepted: 10 November 2018; Published: 15 November 2018



Abstract: A research and technological challenge for fuel processors integrated with High Temperature Polymer Electrolyte Membrane Fuel Cells (HT-PEMFCs), also known as Internal Reforming Methanol Fuel Cells (IRMFCs), operating at 200–220 °C, is the development of highly efficient catalysts, which will be able to selectively (low CO and other by-products formation) produce the required quantity of hydrogen at these temperatures. In this work, various amounts of platinum were dispersed via deposition-precipitation (DP) and impregnation (I) methods onto the surface of hydrothermally prepared ceria nanorods (CNRs) and titania nanotubes (TNTs). These nanostructured catalysts were evaluated in steam reforming of methanol process targeting the operation level of IRMFCs. The (DP) method resulted in highly (atomically) dispersed platinum-based catalysts, as confirmed with Scanning Transmission Electron Microscopy (STEM) analysis, with a mean particle size of less than 1 nm in the case of 0.35 wt.% Pt/CNRs catalyst. Ultra-fine dispersion of platinum species correlated with the presence of oxygen vacancies, together with the enrichment of CNRs surface with active metallic phase resulted in a highly active catalyst achieving at 220 °C a hydrogen production rate of 5500 cm³ min⁻¹ per g of loaded platinum.

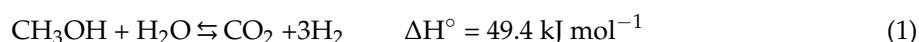
Keywords: steam reforming; methanol; hydrogen; fuel cell; platinum catalysts; ceria; titania

1. Introduction

Methanol is an attractive energy source for portable and off-grid power applications, since it: (i) overcomes batteries or fuel cells fed with pure, stored H₂, in terms of energy density; (ii) has low sulphur content; (iii) can be easily handled/stored/transferred; (iv) can be reformed to hydrogen-rich gas mixtures at low temperatures (<250 °C); and (v) with low CO production. The latter is a severe poison for Low-Temperature Polymer Electrolyte Membrane Fuel Cells (LT-PEMFCs) and must be removed usually via Water-Gas-Shift (WGS: CO + H₂O = CO₂ + H₂) and Preferential CO Oxidation (PROX: CO (or H₂) + 1/2O₂ → CO₂ (or H₂O)) catalytic processes to less than 100 ppm. However, if the fuel cell can operate at high temperatures (160–220 °C), which is the case for High Temperature Polymer Electrolyte Membrane Fuel Cells (HT-PEMFCs), then the WGS reactor can be eliminated. Moreover, this type of fuel cell can also tolerate high concentrations of CO, as high as 2 vol.%, in the reformed hydrogen-rich gas stream, thus making the methanol fuel processor more simple and lighter in weight and volume, since both WGS and PROX catalytic reactors and the accompanied heat exchangers and

other peripherals will not be necessary [1,2]. Recently, Avgouropoulos et al. [1–5] demonstrated the functionality of an Internal Reforming Methanol Fuel Cell (IRMFC), where the methanol gets reformed by a Cu-based catalyst incorporated into the anode compartment of HT-PEMFC. This option offers more room for simplification of the design and control of a compact power unit, which will be very attractive for portable and off-grid applications.

Steam Reforming of Methanol (SRM) is an endothermic catalytic process that provides at relatively low temperatures (<250 °C) and ambient pressure, a hydrogen-rich gas stream (hydrogen up 75%) with low CO concentration (usually around 1–2%; mainly produced via methanol decomposition or/and reverse-WGS, thus diminishing hydrogen selectivity of SRM process) [6–9]:



Other by-products, such as methane, formaldehyde, methyl formate and dimethylether can also be present at ppm level in the outlet gas stream of the methanol processor. Operation of the fuel cell at high temperatures allows the utilization of “low quality” reformat gas streams, however elimination of these by-products is in advantage of the hydrogen selectivity. Therefore, highly efficient methanol reforming catalysts should be developed, matching the operation level of IRMFC (i.e., 200–220 °C). Towards this aim the research community employs new chemical synthesis methods for the preparation of nanostructured catalysts with high selectivity, extremely high activity, low energy demands and long-life time [4,5,10–12]. These properties can be achieved only by controlling the size, the shape, the particle size distribution, the composition and the electronic structure of the surface, the thermal and chemical stability of the specific nanocomponents.

Two different families of catalytic systems have been studied in methanol reforming: (i) Cu- [4,5,8–30] and (ii) noble metal-based catalysts [8,31–47]. Cu-based metal oxides, such as the commercially available Cu/ZnO(Al₂O₃), as well as Cu-Ce and Cu-Mn(Al) mixed oxides, have been extensively investigated in SRM, due to their low cost, high activity and low CO selectivity. Despite the fact that Cu/ZnO(Al₂O₃) catalysts are used in large H₂ plants, there are several drawbacks that limit their application in mobile and portable fuel cell power units. Moreover, copper-based catalysts require a pre-reduction step in order to be activated and a post-passivation step in order to avoid pyrophoricity phenomena if highly dispersed metallic copper is exposed in air. These catalysts also have poor thermal stability above 300 °C and limited long-term stability under reaction conditions.

On the other hand, noble metal-containing catalysts, especially Pd/ZnO [8,31–47], have been the subject of extensive research in SRM. In contrast with copper-based catalysts, the presence of noble metal offers long term stability and no pyrophoric behaviour. Moreover, the production of CO is suppressed to levels similar with copper-based catalysts, if PdZn alloy active species are predominant on the catalytic surface. Nevertheless, their cost is still a limiting parameter for practical fuel cell applications and alternatively, further research is necessary in order to develop highly efficient catalysts with ultra-low noble metal loadings. The goal of reducing the amount of precious metals in various catalytic processes, especially in hydrogen-related technologies, is closely related with the growing research interest in atomically dispersed catalytic sites, where the theory of strong metal-support interactions has been “re-activated,” offering strong arguments on how clusters of precious metals (such as platinum and gold) with very small size, even atomically dispersed, are stabilized on various reducible supports, such as ceria, resulting in catalytically active and stable arrangements for various reactions [48–50]. In this context, a general way for enhancing the catalytic activity of materials oxides takes advantage of the synergistic effect at the interface between two phases, while recent development of morphology-controlled synthesis of nanostructured materials, via non-conventional chemical routes, such as hydrothermal method in alkali solutions, indicate that catalysts with well-defined reactive sites may be designed [51–53].

TiO₂ and CeO₂ are attractive reducible metal oxides used as supports for the active metal nanoparticles of heterogeneous catalysts and are well known to influence the catalytic activity through strong metal–support interactions. The strong interaction leads to the stabilization of small metal

particles through a wider contact area and often gives the longest perimeter interface around them. These oxides play an important role in the catalysis by precious metals providing additional sites at the interface for the adsorption of the reactants close to the precious metal sites. Nanostructured titania materials show high photocatalytic activity and are widely used as a catalyst and carrier of catalysts in various reactions where the tuning of the pore size and overall morphology are crucial [54,55]. It is inferred that a catalyst based on TiO_2 with different structures might exhibit different physicochemical properties and catalytic activities. Titania nanotubular structure offers significant advantages which seem to be related to the property that a high value of specific surface area and structural peculiarities increase the number of potentially active centres in the nanotubes.

Ceria with its distinct defect chemistry and the ability to exchange lattice oxygen with the gas phase offers a unique catalytic support which promotes active metal dispersion and enhances the catalytic activity at the metal–support interface [30,34,51–53,56,57]. The type, concentration and distribution of oxygen vacancies dominate the redox properties of ceria-based materials, accounting for the final performance of catalysts. Moreover, strong metal–support interactions, which depend strongly on the morphology or exposed surface planes of the supports, may significantly promote the activity and selectivity induced. The exposed surface of CeO_2 can be enriched with oxygen vacancies, where the metal nanoparticles or nanoclusters bind strongly [3–5,12–14]. Recent studies have demonstrated the high impact of surface nanostructuring on the performance of ceria and titania as supports of precious metals [51–57]. Surface crystallography can affect the final electronic state and catalytic performance of the deposited active phase and in this respect, there have been intensive research efforts in the investigation of the structure sensitive behaviour of ceria-based catalytic systems [29–42]. Recent reports have confirmed the strong shape/crystal plane effect of CeO_2 in various catalytic reactions, such as CO oxidation and water-gas-shift [48–53].

In view of the IRMFC energy applications, research efforts on methanol reforming catalysts should focus on their: (i) activity at $\sim 200\text{--}220$ °C and (ii) ability to avoid pre-activation treatments [1–5,10–12]. In this work, the main idea was to develop low-loading platinum-based catalysts, which will have high activity and selectivity in SRM reaction, in order to be potentially used as anode electrocatalysts in high-temperature PEM fuel cells offering great cost savings as compared with typical fuel processor-fuel cell systems. The fact that the electrocatalyst will be able to (i) reform methanol and at the same (ii) oxidize hydrogen (bifunctional operation), will be of high importance, since the operation characteristics of the fuel cell change significantly in the presence of small amounts of unconverted methanol in the H_2 stream due to the poisoning effect of adsorbed methanol on the electrocatalyst and the proton conductivity of the membrane [4,5,12]. Here, a hydrothermal, synthesis route was applied for the preparation of titania nanotubes (TNTs) and ceria nanorods (CNRs) as catalyst supports. Platinum nanoparticles were finely dispersed on the oxide nanostructures via wet impregnation (I) and deposition precipitation (DP) methods. The catalytic activity and selectivity of Pt/ TiO_2 and Pt/ CeO_2 nanomaterials was evaluated in the steam reforming of methanol and correlated with the physicochemical properties, characterized with various techniques, thus demonstrating their functionality in the title process.

2. Results and Discussion

2.1. Chemical Analysis (XRF)

Metal composition of all the Pt/TNTs and Pt/CNRs catalysts, determined by X-ray fluorescence (XRF) technique, is shown in Tables 1 and 2, respectively. These values are almost identical to the corresponding nominal values in the case of the impregnated samples, while filtration of the (DP) pastes resulted in approximately 20% lower platinum loadings.

Table 1. Physicochemical characteristics of Pt/TNTs catalysts prepared by both impregnation (I) and deposition precipitation (DP) method.

Sample	Pt Loading ^a (wt.%)	Pt Loading ^b (wt.%)	S _{BET} (m ² /g)	V _P (cm ³ g ⁻¹)	d _{Pt (111)} (nm) ^c	d _{TNTs (020)} (nm) ^d
TNTs	-	-	199.3	0.49	-	12.7
Pt/TNTs (I)	3.0	2.97	170.1	0.42	6.9	15.3
Pt/TNTs (DP)	3.0	2.35	193.3	0.48	n.o.	11.3

^a Nominal loading; ^b Metal composition determined by XRF analysis; ^c Estimated by the Scherrer equation applied to the (111) reflection of Pt; ^d Estimated by the Scherrer equation applied to the (020) reflection of TNTs.

Table 2. Physicochemical characteristics of Pt/CNRs catalysts prepared by both impregnation (I) and deposition precipitation (DP) method.

Sample	Pt Loading ^a (wt.%)	Pt Loading ^b (wt.%)	S _{BET} (m ² /g)	V _P (cm ³ g ⁻¹)	d _{Pt (111)} (nm) ^c	d _{CeO₂ (111)} (nm) ^d
CeO ₂	-	-	88.2	0.19	-	10.08
Pt/CNRs (I)	3.0	3.02	100.8	0.36	n.o.	10.17
Pt/CNRs (DP)-low ^e	0.35	0.30	107.5	0.41	n.o.	9.68
Pt/CNRs (DP)	3.0	2.45	114.2	0.43	n.o.	8.9

^a Nominal loading; ^b Metal composition determined by XRF analysis; ^c Estimated by the Scherrer equation applied to the (111) reflection of Pt; ^d Estimated by the Scherrer equation applied to the (111) reflection of CNRs; ^e Low denotes low loading of platinum.

2.2. Microscopic Analysis (SEM, TEM, STEM, EDX)

Hydrothermal treatment of TiO₂ (Degussa P25) powder resulted on the formation of Titanium Nanotubes (TNTs) with an outer diameter of 8–10 nm and a length of 20–50 nm, as it can be observed in the SEM (Scanning Electron Microscopy), TEM (Transmission Electron Microscopy) and STEM (Scanning Transmission electron Microscopy) images presented in Figure 1. The ends of the nanotubes are open, while the inner channel is unblocked and the walls, of approximately 1 nm thickness, are quite smooth. Hydrothermally prepared TNTs with similar diameter size and lengths varying from 20 up to a few hundreds of nanometres, have been also reported by other groups [58–60]. The structure of TiO₂ remains stable after calcination at 400 °C, however, it has been reported that higher calcination temperatures (>500 °C), result in fractured nanotubes with dramatically lower surface area [58]. In this work the morphology of the TNTs is maintained very well up to 3 wt.% of Pt loading regardless the method used (I or DP), as it can be confirmed with electron microscopy analysis (Figure 2). Pt nanoparticles are distinguished as dark dots in the TEM images and as bright dots in the STEM ones. The dispersion of platinum nanoparticles onto the surface of TNTs is fine and uniform in both synthesis methods, though the mean particle size is different (Figure 2e,f). A mean metal particle size of 2.6 nm was obtained in the case of Pt/TNTs (I) catalyst, while the corresponding size is smaller, that is, 1.5 nm, for (DP) sample. The bigger platinum particle size of the impregnated sample was also confirmed by the EDX (Energy-dispersive X-ray) micrographs, presented in Figures S1 and S2.

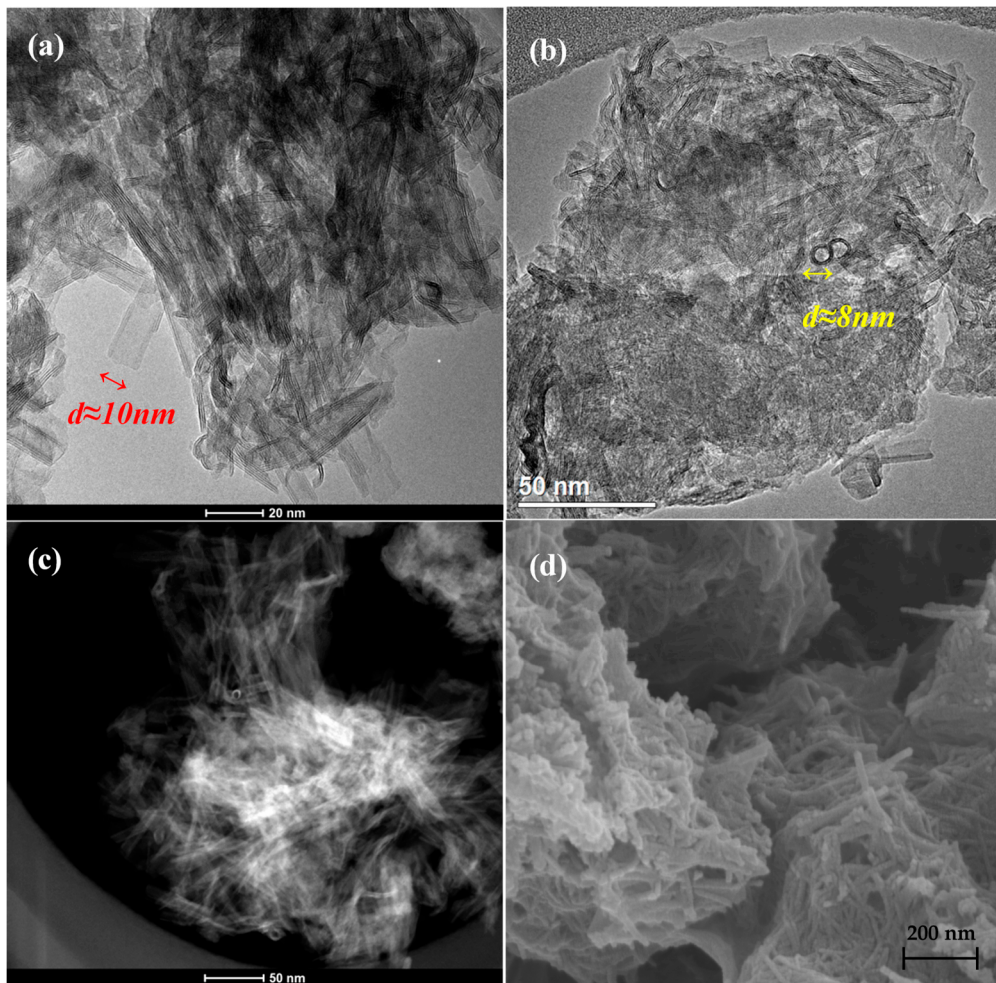


Figure 1. TEM (a,b), STEM (c) and SEM (d) images of TNTs after calcination at 400 °C.

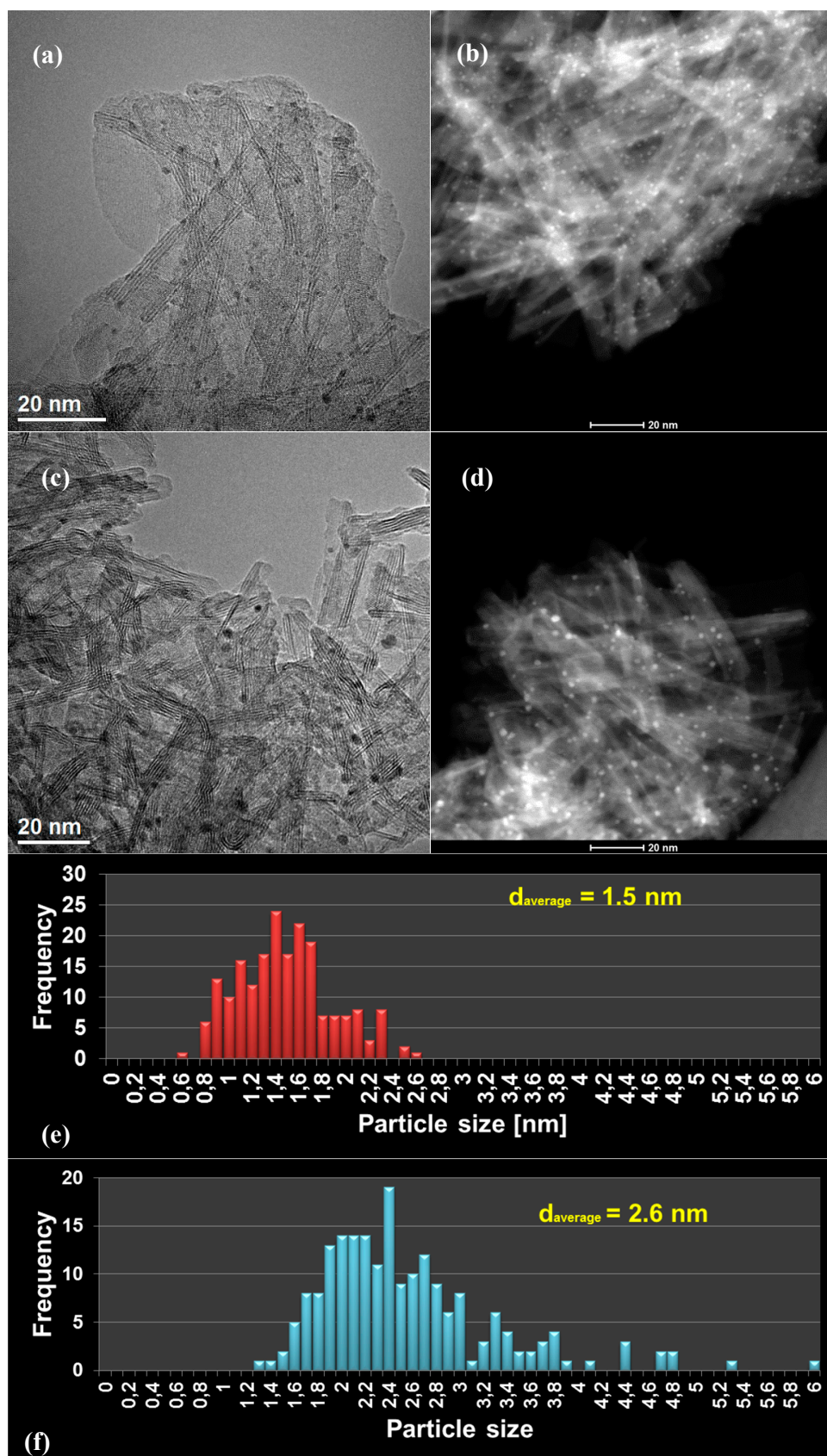


Figure 2. TEM (left), STEM (right) images and particle size distribution (bottom) of reduced Pt/TNTs prepared by deposition-precipitation (a,b,e) and impregnation (c,d,f) methods.

Hydrothermal method was also applied in order to prepare the CeO₂ nanostructured substrate. This chemical route resulted in the formation of ceria nanorods (CNRs), as it can be confirmed via SEM, TEM and STEM images shown in Figure 3.

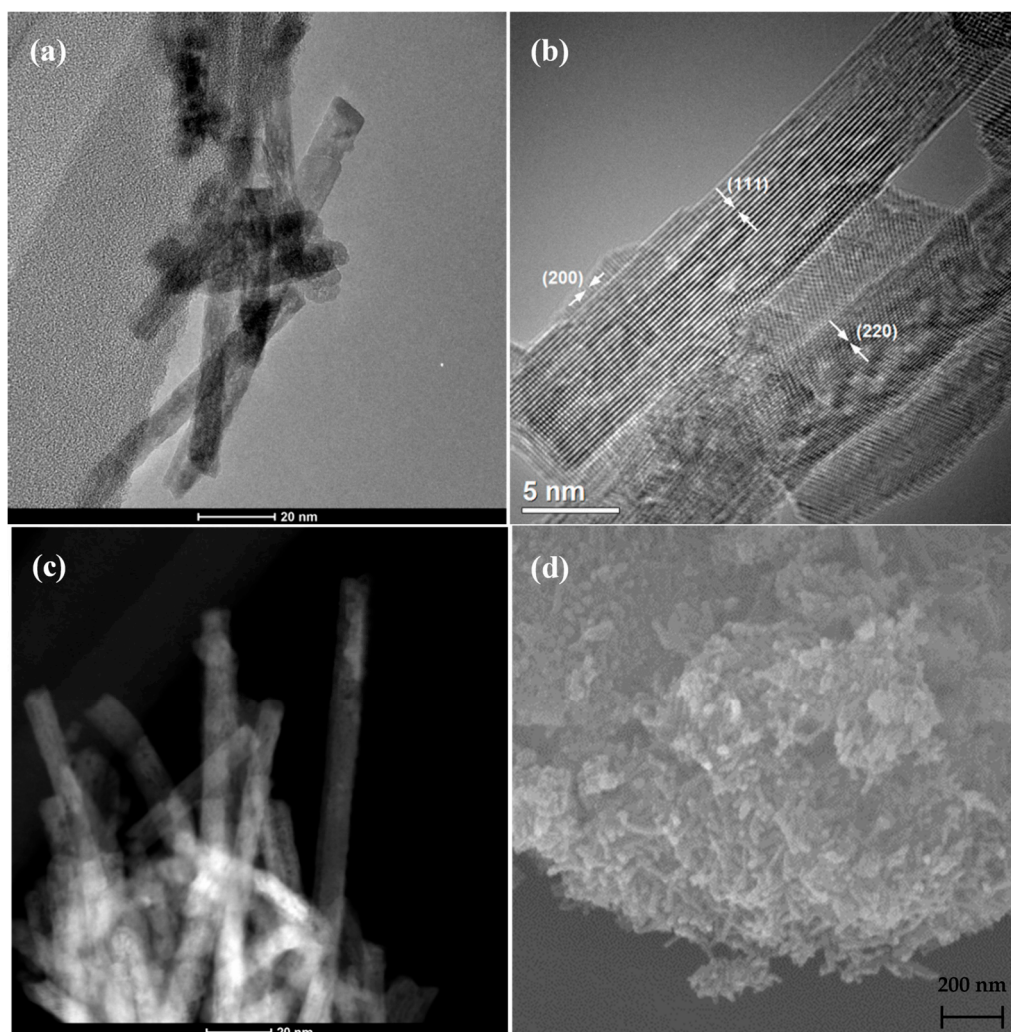


Figure 3. TEM (a,b), STEM (c) and SEM (d) images of CNRs after calcination at 400 °C.

TEM images revealed a mean width of 5–7 nm for CNRs, while their length varies from 100 up to 150 nm, in line with the literature [61–64]. The outer surface of the nanorods seems quite rough with small defects (pores), probably due to oxygen vacancies. These defects are disclosed in the TEM images as low contrast regions, while in the STEM images as darker areas, indicating lower mass in these regions. It has been reported [61,65] that these features could arise from voids in the nanostructure or surface steps. This defective surface is believed to provide enriched nucleation sites for the growth and the improved dispersion of the loaded metal nanoparticles. On this basis, Tao et al. [66] used plasma etching to create such defects on the as-prepared ceria substrate. Herein, since the aspect ratio of length to width is above 15, the primary exposed surface of ceria is along the length of the rods; hence rods expose their (111) planes, as it was observed in most of the obtained images. Facet (220) is observed in Figure 3b, indicating that the growth direction of the nanorods is the (110), in accordance with the literature [61,67,68]. Apart from the predominant (111) facet, (200) can be also distinguished in few cases, as also reported in the literature for hydrothermally synthesized CNRs [69,70]. Similarly to the TNTs, 3 wt.% Pt was also dispersed onto the surface of CNRs via impregnation and deposition precipitation methods. Moreover, a catalyst with very low loading of platinum (i.e., 0.3 wt.%) was also prepared by (DP) method.

The morphology of Pt/CNRs was also characterized with electron microscopy (Figures 4 and 5). The structure of the substrate has not been affected by the addition of platinum via both methods. The nanorods nature is maintained and the aforementioned defects are still visible in all the samples. Due to the low metal loading, the ultra-fine dispersion of Pt species and the low contrast with ceria, it was difficult, even with HRTEM (High Resolution TEM), to distinguish these species and obtain a particle size distribution. A closer look at the STEM images in Figure 5, few platinum nanoparticles with an atomic size (<1 nm) can be revealed. It is worth noting that this is also the size of the defects (dark round areas). This confirms the correlation proposed by many groups, between ultra-fine metal dispersion and surface defects (oxygen vacancies). This uniform and ultra-fine dispersion of Pt nanoparticles was also verified by EDX analysis shown in Figures S3 and S4.

2.3. Surface Area, Pore Size and Particle Size (N_2 Isotherms, XRD)

The specific surface areas for all the substrates and the Pt-loaded samples are summarized in Tables 1 and 2. The N_2 isotherms and the pore size distribution of all the samples are shown in Figures S5–S8. In the case of TNTs, a surface area of ca. $200 \text{ m}^2 \text{ g}^{-1}$ was obtained by the hydrothermal method, almost 5 times higher than the surface area of the mother material of TiO_2 P25 powder, which was used as a precursor. This surface area was maintained after both (I) and (DP) methods, even though these samples were calcined at $400 \text{ }^\circ\text{C}$. The deposition of Pt nanoparticles did not block the pores of the nanotubes, as suggested by the mean pore size values. In the case of CNRs samples, the deposition of Pt onto the surface of the nanorods increased both the surface area and the pores of the samples. Similar findings were observed by other groups under similar synthesis conditions [58,71]. Pure CNRs had a specific surface area of $88 \text{ m}^2 \text{ g}^{-1}$, while the Pt loaded catalysts showed increased surface area, with both (I) and (DP) methods, as shown in Table 2. This is in accordance to the literature where ceria nanorods were found to have high specific surface areas ($\sim 100 \text{ m}^2 \text{ g}^{-1}$) [62,72]. The nitrogen adsorption-desorption measurements at $-196 \text{ }^\circ\text{C}$ showed type II isotherms with type B hysteresis loops as shown in Figures S5–S8.

Figure 6 shows the XRD (X-ray Diffraction) patterns of Pt-loaded materials together with the pure nanostructured substrates prepared via the hydrothermal method. Crystallite sizes of TNTs, CNRs and platinum metal, as calculated using Scherrer's equation, are reported in Tables 1 and 2. In agreement with Baiju et al. [73], the characteristic diffraction peaks of the monoclinic crystal structure of layered trititanic acid, $\text{H}_2\text{Ti}_3\text{O}_7$ (JCPDS 41-0192), can be clearly identified in the titania substrate, even though it is calcined at $400 \text{ }^\circ\text{C}$. Other groups have reported that hydrogen titanate is transformed into anatase- TiO_2 after calcination at such temperatures [58]. Treatment of TNTs with H_2PtCl_6 during (I) method, leads to the formation of NaCl, as revealed in Figure 6. Remaining Na^+ ions from the washing step following the hydrothermal treatment of TiO_2 , reacted with the Cl^- ions from the metal precursor to form NaCl. Additionally, in the case of the impregnated sample, Pt (111) peak can be observed, corresponding to a mean Pt particle size of $\sim 7 \text{ nm}$, as calculated using Scherrer's equation. This is in accordance with the TEM measurements, where a small number of Pt particles were measured to have a size of 6 nm , while the mean size was calculated to be 2.6 nm . In the catalysts prepared via the (DP) method, no other phase apart from hydrogen titanate was observed, since Pt was finely dispersed and the size of Pt nanoparticles was too small, as confirmed by TEM analysis. For the pure CNRs and the Pt/CNRs catalysts, distinct fluorite-type oxide structure of CeO_2 (JCPDS 81-0792) is present in the diffraction patterns. Platinum nanoparticles were highly dispersed on the surface of ceria nanorods via (I) and (DP) methods, thus no detectable diffractions of platinum metal crystallites could be distinguished at loadings lower than 3 wt.%. In this respect, platinum species may be considered to be in highly dispersed form in these samples with primary crystallite sizes less than $\sim 1\text{--}2 \text{ nm}$, in agreement with TEM analysis. Especially for the 0.35%Pt/CNRs catalyst, a small shift is observed in the CeO_2 (111) diffraction peak, which implies the distortion of the cell by incorporation of Pt nanoparticles into the lattice.

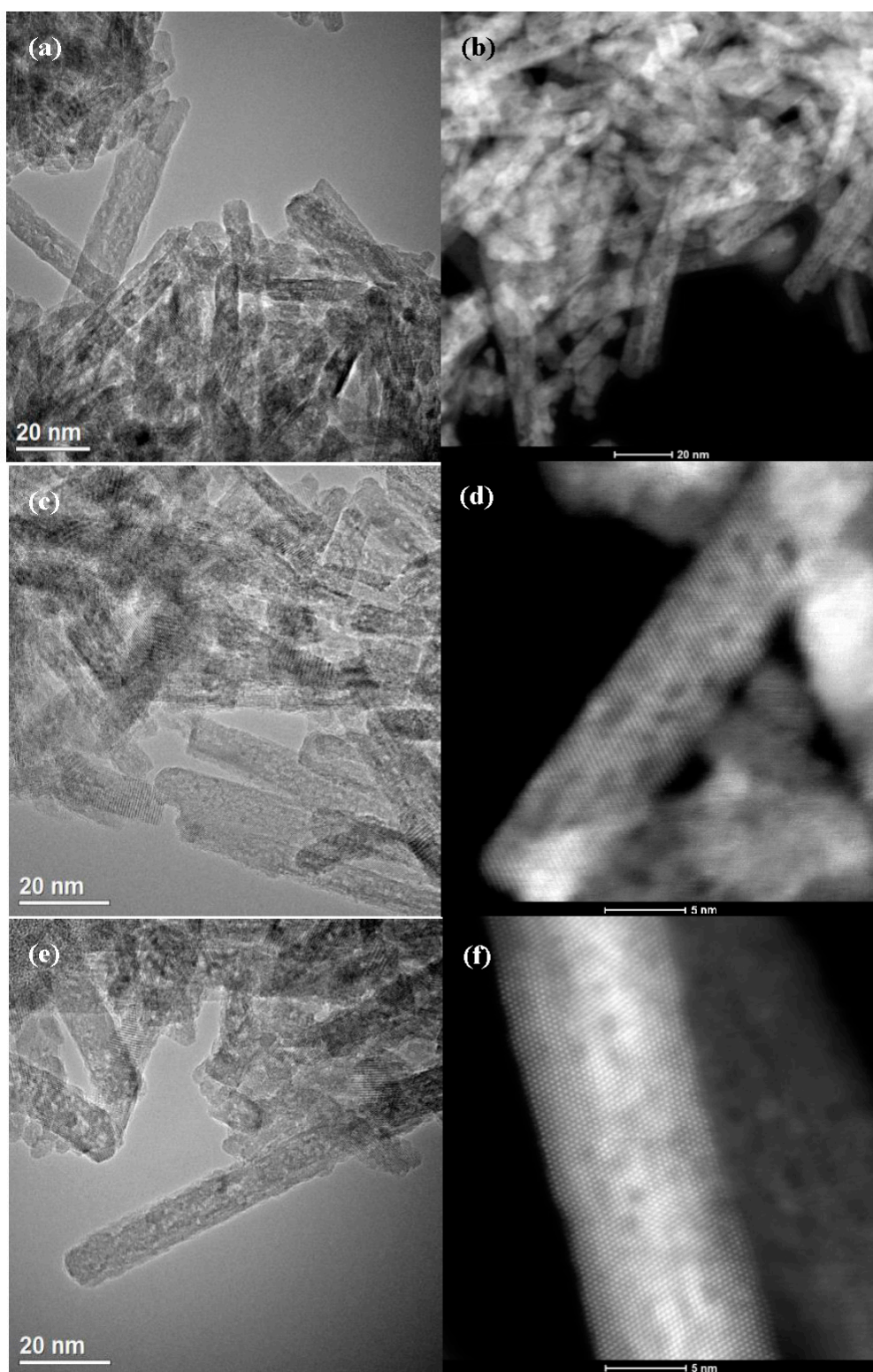


Figure 4. TEM (left), STEM (right) images of reduced Pt/CNRs prepared by (I) (a,b) and (DP) (c,d) methods. The (DP) catalyst prepared with low Pt loading is depicted in (e,f).

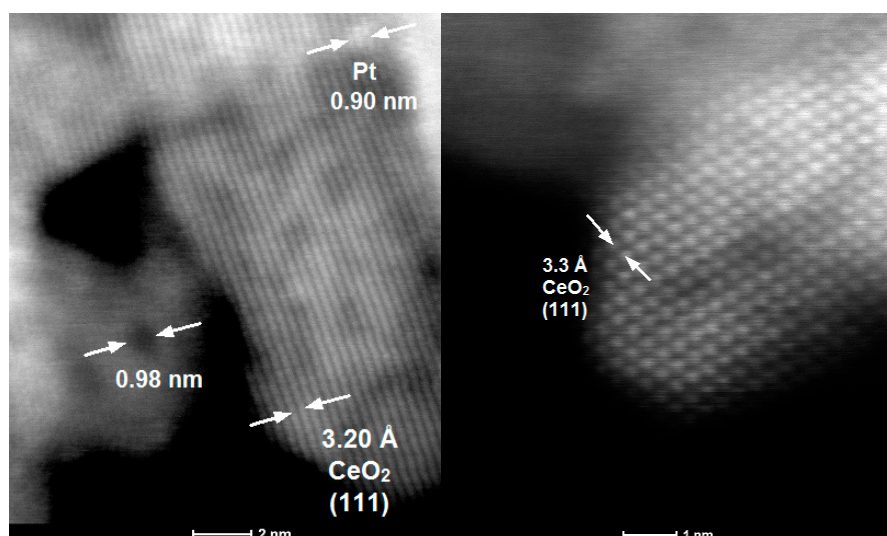


Figure 5. STEM images of reduced 3% Pt/CNRs (DP) catalyst. Defects, Pt nanoparticles and CeO₂ (111) lattice fridges, are pointed out with arrows.

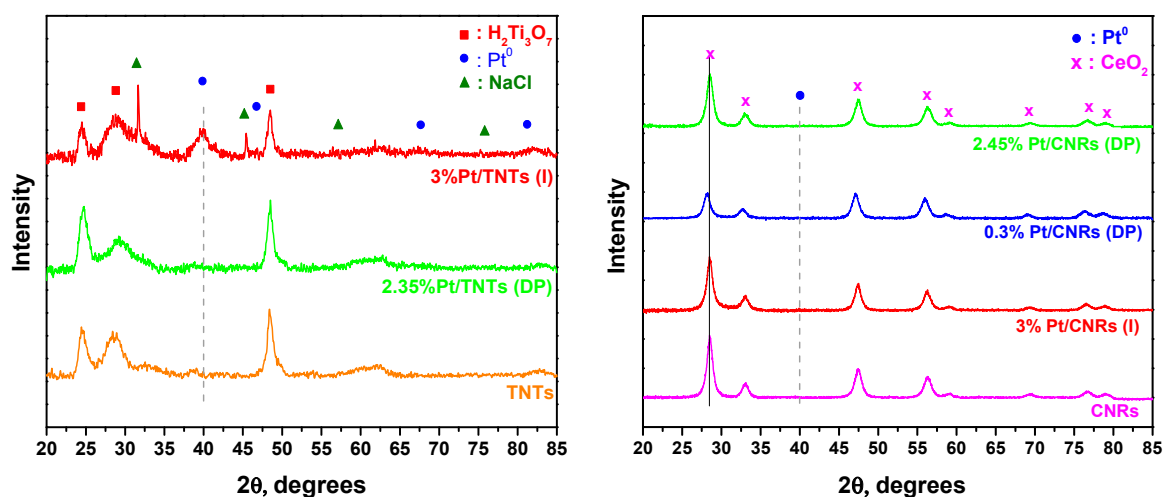


Figure 6. XRD patterns of Pt/TNTs (left) and Pt/CNRs (right) catalysts prepared with (DP) and (I) methods. Pure substrates are also presented for comparison reasons.

2.4. Raman Analysis

Raman spectroscopy was applied in order to distinguish among different titania polymorphs as well as to receive some surface information about the defect sites in CeO₂. As can be observed in Figure 7a, Raman spectra of the pure TNTs is consisted of the characteristic Raman bands of anatase phase at 144, 393, 513 and 638 cm⁻¹ coexisting with Raman vibrations at 195, 280, 450 cm⁻¹ and three weak broad bands at 650–710, 800–840 and 900–930 cm⁻¹, characteristic of the hydrogen titanate nanotubes [74,75]. Titanate phase is associated with the Ti–O–H (278 cm⁻¹) and Ti–O–Ti (450 cm⁻¹) bond. The three broad bands above 600 cm⁻¹ are related to surface vibrational modes [75]. Deposition of Pt nanoparticles onto the surface of TNTs did not alter the structure of the support, as all bands assigned to the titanate phase are still observed in the Raman spectra. On the contrary, the intensity of the Raman bands corresponding to anatase phase decreased after platinum addition and took the lowest value in the impregnated sample. Similar findings were observed by Toledo-Antonio et al. [74], who reported that Raman bands corresponding to anatase, strongly decreased upon Ir and Pt–Ir addition, suggesting that this phase, or the vibrating bonds of the structure are being extinguished by the presence of highly dispersed particles on the surface.

Analysis of the Raman spectra of CNRs and Pt/CNRs (Figure 7b) confirmed the presence of the cubic fluorite structure via the characteristic Raman bands at 260, 461, 592 and 1150–1200 cm^{-1} . It is well documented that the main band at 461 cm^{-1} is attributed to the Raman-active vibrational mode (F_{2g}) of fluorite type structure, while the band at 592 cm^{-1} is considered to be the band of the defect-induced (D) mode and the last broad band is a second-order longitudinal optical (2LO) mode [62,70,76]. Concerning the weak band at 833 cm^{-1} , it has been reported in the literature that it is observed on ceria samples after reduction in H_2 streams and was assigned to the $\nu(\text{O}-\text{O})$ stretching vibration of peroxo species $(\text{O}_2)^{2-}$ formed on ceria [77,78].

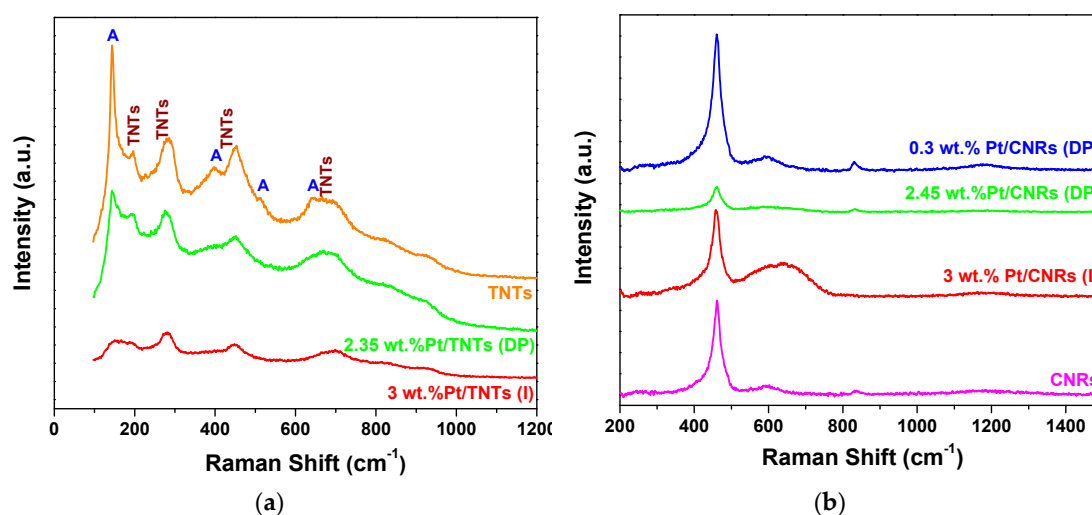


Figure 7. Raman spectra of Pt/TNTs (a) and Pt/CNRs (b) catalysts prepared with DP and I methods. Pure substrates are also shown for comparison reasons.

Addition of Pt with different loadings via various chemical routes resulted in changes in the corresponding Raman spectra. When (DP) method was employed, all four bands assigned to the fluorite type structure were still apparent, not shifted and with no other new bands added. In the case of 3%, all intensities were dramatically decreased, while in the case of 0.3 wt.% only the F_{2g} band was slightly increased. After Pt addition via (I) method, a new broad band (consisting of two bands at ~ 560 and 650 cm^{-1}) appeared at $580\text{--}660 \text{ cm}^{-1}$. Tong et al. [70] reported that after calcination of Pt/ CeO_2 nanorod catalysts, synthesized by the same technique, two additional Raman bands appeared at 550 cm^{-1} and 665 cm^{-1} . They attributed them to the strong interaction between PtO_x and CeO_2 , so they assigned them to Pt–O–Ce and Pt–O bands, respectively. They demonstrated that after reduction of the catalysts, under similar conditions to the ones we apply here, these two bands partially remained present.

2.5. XPS Analysis

X-ray photoelectron spectra (XPS) of Pt 4f, Ti 2p, Ce 3d and O1s core level regions of Pt/CNRs and Pt/TNTs catalysts with various platinum loadings were collected. The regional spectra of Pt 4f were deconvoluted into two or three sets of spin orbital doublets, depending on the oxidation state of the noble metal. As shown in Figure 8, a negative shift of $\sim 0.5 \text{ eV}$ is observed in the Pt 4f spectra for both the Pt/TNTs samples. XPS peaks at 70.7 and 74.0 eV are attributed to Pt^0 in comparison to the binding energy of 71.2 and 74.3 eV for bulk metallic Pt, while the peaks located at 72.8 and 76 eV, attributed to Pt^{2+} . In agreement with the literature, this negative shift resulted from the electron transfer from TiO_2 to Pt [79–82]. Surface elemental composition and chemical state of Pt/TNTs are listed in Table 3. It can be noted that both catalysts have almost the same surface concentration of metallic platinum and total platinum species, the latter expressed as Pt/(Pt + Ce) ratio, even though the applied nominal ratio is a little bit different.

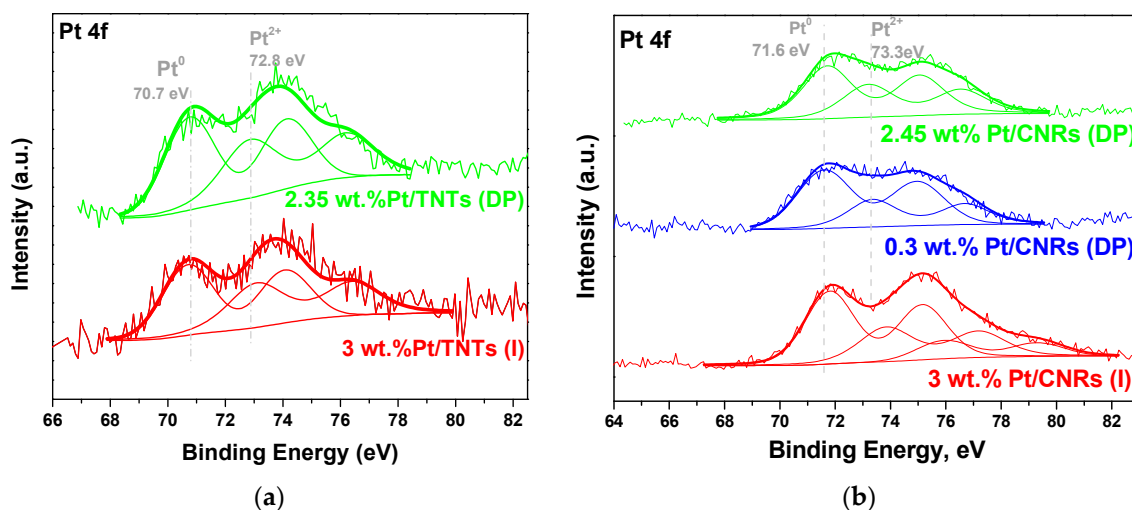


Figure 8. XPS of Pt 4f core level regions of Pt/TNTs (a) and Pt/CNRs (b) catalysts.

The negative shift observed at the XP spectra of Pt/TNTs catalysts is not the case for the Pt/CNRs samples. On the contrary, metallic Pt for Pt/CNTs (DP) samples, is observed at a binding energy of 71.8 eV, which is higher than the typical binding energy for metallic platinum. Analysis of these spectra suggested the presence of partially positive charged platinum ($\text{Pt}^{\delta+}$), in agreement with a previous report for XP spectra of Pt 4f on CeO_2 nanorods [70]. Accordingly, Pt^{2+} XPS peaks are also shifted to higher binding energies, that is, at 73.6 eV. Loading platinum on CNRs via (I) affected in a different way the surface chemical state of the catalyst. Not only the XPS peaks assigned to Pt^0 and Pt^{2+} species are shifted at even higher binding energies but one more chemical state of platinum can be distinguished and this is Pt^{4+} . It has to be underlined that Raman analysis of Pt/CNRs (I) catalyst indicated the co-existence of Pt–O–Ce and Pt–O bands. The surface elemental composition of the Pt/CNRs samples is shown in Table 3. In line with the Raman analysis for the CNRs-based samples, the impregnated one exhibits the lowest surface Pt^0 amount and the lowest Pt/(Pt + Ce) ratio. (DP) method promoted the enrichment of the CNRs surface with platinum species, while ultra-low loaded catalyst contains even more metallic platinum species. These results are expected to play a significant role in the catalytic activity and selectivity in the steam reforming of methanol.

Table 3. Nominal and XPS calculated, elemental composition of Pt/TNTs, Pt/CNRs (I) and (DP) catalysts, expressed as Pt/(Pt + Ce).

Catalyst	Nominal	XPS	Pt^0
3% Pt/CNRs (I)	0.027	0.010	55.3%
0.35% Pt/CNRs (DP)	0.002	0.080	67.0%
3% Pt/CNRs (DP)	0.020	0.049	60.7%
3% Pt/TNTs (I)	0.012	0.010	55.6%
3% Pt/TNTs (DP)	0.007	0.010	56.0%

2.6. Catalytic Activity/Selectivity

The catalytic activity and selectivity of Pt/CNRs and Pt/TNTs catalysts for the steam reforming of methanol are presented in Figure 9 and Table 4. For all the catalysts tested in the temperature region of 190–220 °C, the main products of SRM were H_2 and CO_2 , while CO was also produced in significant concentrations. Other by-products such as methane, formaldehyde and methyl formate were also formed in much smaller quantities and were favoured by the reaction temperature and/or low reaction temperatures and/or low methanol conversions. High CO selectivity implies higher activity of these catalysts for the decomposition of methanol or/and the reverse water-gas shift reaction. We should note that in the case of HT-PEMFCs, the employed membrane-electrode-assemblies can tolerate up to

2%, or even higher concentrations of CO, depending on the water and methanol content in the anode feed stream [5,12,83–85] and this is an advantage of this type of fuel cells. Under our experimental conditions, CO selectivity was much higher than its equilibrium value in water-gas shift reaction, suggesting that CO was also a primary product of methanol steam reforming, produced mainly via methanol decomposition, while reverse WGS reaction might also take place, especially at higher temperatures. Nevertheless, these concentrations of produced CO were kept in the range of 0.5–3.5%, which can be tolerated from HT-PEMFCs operating at such high temperatures (i.e., 200–220 °C). Higher methanol conversions and hydrogen yields were obtained over the CNRs-based catalysts, while the (DP) method resulted in more efficient samples, as compared with the wet-impregnation method. Highly dispersed catalysts were synthesized with both techniques, however the former method favoured the formation of smaller platinum nanoparticles, which were atomically dispersed over the surface of ceria nanorods, in agreement with S/TEM and XPS analysis.

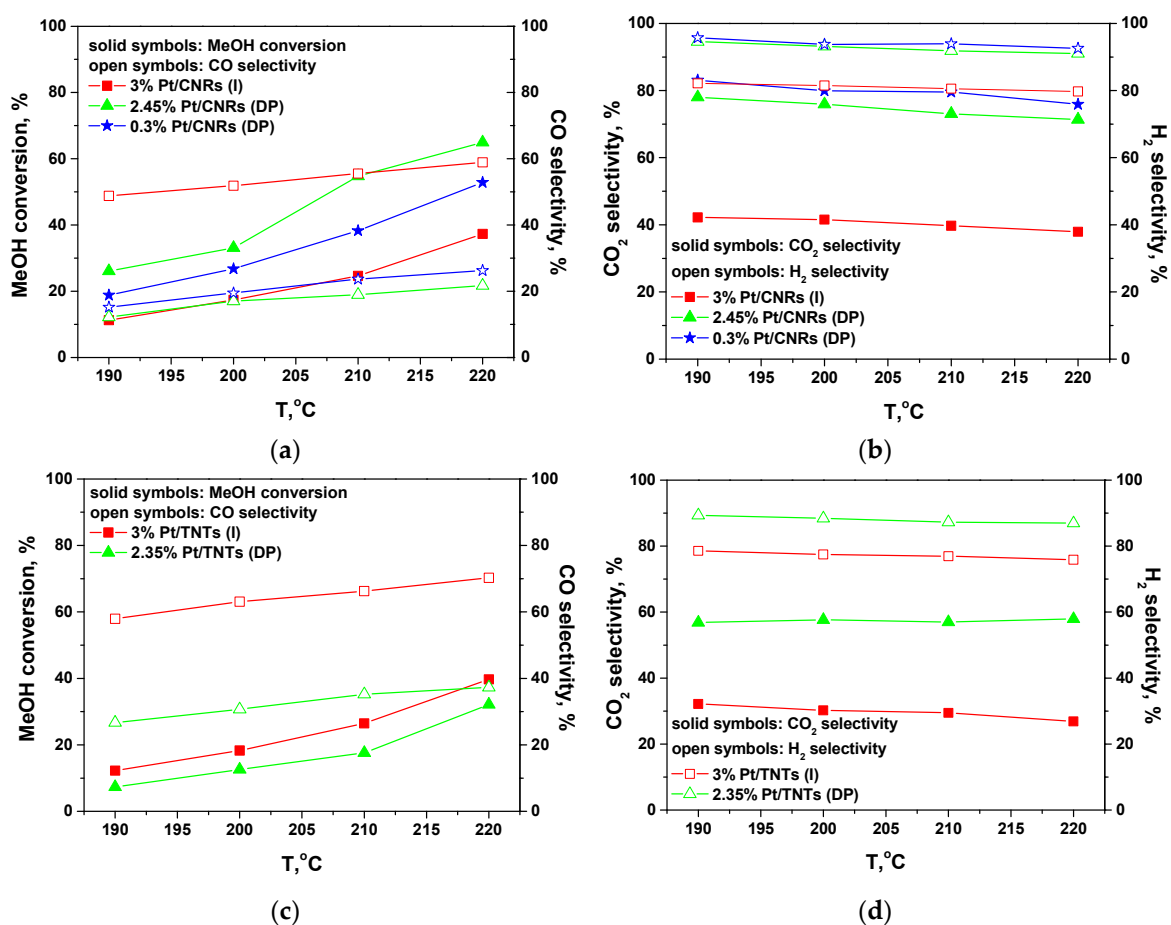


Figure 9. Activity and selectivity for SRM process over Pt/CNRs (a,b) and Pt/TNTs (c,d) catalysts.

Table 4. Activity and selectivity for SRM reaction¹ over Pt/CNRs and Pt/TNTs catalysts.

Catalyst	Pt Content	MeOH	CO	H ₂	H ₂ Production Rate	
	wt.% ²	Conversion, %	Selectivity, %	Selectivity, %	cm ³ /min/g _{cat}	cm ³ /min/g _{Pt}
Pt/CNRs (I)	3.02	37.3	58.9	79.7	10.0	331.1
Pt/CNRs (DP)	2.45	65.0	21.7	92.6	20.5	836.7
Pt/CNRs (DP)	0.3	53.4	26.2	91.0	16.5	5500.0
Pt/TNTs (I)	2.97	40.2	70.3	76.0	10.2	343.4
Pt/TNTs (DP)	2.35	32.6	37.3	87.0	7.0	297.9

¹ Conversion, selectivity and reaction rate values obtained at T = 220 °C. ² determined by XRF.

Atomic dispersion promoted the metal-support interactions and this is depicted in the Pt/CNRs (DP) catalyst with ultra-low loading of 0.3 wt.% for platinum, where similar methanol conversion and selectivity were achieved in comparison with the 2.45 wt.% Pt/CNRs (DP) catalyst. As discussed above, and considering the Raman analysis for the CNRs-based catalysts, the (DP) samples exhibit higher amount of surface Pt⁰ species and also higher Pt/(Pt + Ce) ratio. Among these samples, the ultra-low loaded catalyst contains even more metallic platinum species. Moreover, if the reaction rate for the production of hydrogen is expressed per g of loaded platinum (Table 4), then a value of 5500 cm³ min⁻¹ g⁻¹_{Pt} was achieved at 220 °C for the former catalyst, which is 7–18 times higher as compared with the other synthesized catalysts.

3. Materials and Methods

3.1. Synthesis of Catalysts Supports

Ceria nanorods (CNRs) and titania nanotubes (TNTs) were prepared by hydrothermal method using (a) Ce(NO₃)₃·6H₂O (Aldrich, Darmstadt, Germany) and (b) TiO₂ P25 powder (Degussa, Frankfurt, Germany) as precursors and NaOH (Alfa Aesar, Karlsruhe, Germany) as precipitating agent [64,72]. Both cerium and titanium reagents were diluted in specific amounts of triple distilled water and then mixed with appropriate aqueous NaOH solutions (C_{NaOH}: 6 M and 10 M, respectively) in a Teflon container. After stirring of the solution for 20 min, the vessel was sealed in a laboratory made stainless steel autoclave and heated at 100 °C (for CNRs) and 120 °C (for TNTs) for 24 h and 48 h, respectively. The resulting paste was washed several times with 3D water until pH = 7, then filtered, dried under vacuum overnight at 70 °C and finally calcined in static air at 400 °C (1 h for TNTs and 4 h for CNRs) in order to obtain the nanostructured catalytic supports.

3.2. Synthesis of Catalysts

Wet impregnation (I) and deposition-precipitation (DP) methods were employed for the deposition of platinum onto the hydrothermally prepared nanostructured supports. Proper amounts of an aqueous solution of H₂PtCl₆·6H₂O and CNRs or TNTs powders were used to yield 0.3–3 wt.% Pt (see Tables 1 and 2; platinum content confirmed via XRF analysis) metal loading in the final catalysts. Regarding (DP) method, a precipitating agent ((NH₄)₂CO₃, Alfa Aesar; 1 M in the case of CNRs and 2 M in the case of TNTs) was added dropwise in the solution of platinum precursor and support, while a constant pH of 9.0 and temperature of ~80 °C were maintained. The precipitates were aged for 4 h at 80 °C, filtered and washed carefully until no chloride ions were present. All the pastes from both preparation methods were dried under vacuum at 80 °C and calcined in air at 400 °C for 2 h. The obtained solids were activated by reduction in flowing 20% H₂/N₂ (100 cm³ min⁻¹) at 300 °C, for 2 h. All the powders were sieved to obtain the desired fraction, with diameter between 90 and 180 μm. This particle size was chosen so that pressure drop, concentration and temperature gradients over the catalyst bed were negligible.

3.3. Catalysts Characterization

The specific surface area (SSA), the pore volume (V_p) and the pore size distribution of the samples were determined from the adsorption and desorption isotherms of nitrogen at –196 °C using a TriStar 3000 Micromeritics Autosorb-1 instrument (Micromeritics, Athens, Greece).

The crystalline structure of the catalysts was analysed by means of an X-ray powder diffractometer (Bruker D8 Advance, Bruker, Birmingham, UK) employing Cu K_α radiation (40 kV, 40 mA), Ni filter and Bragg-Brentano geometry.

X-ray photoelectron spectra (XPS) of Pt-based catalysts were recorded with experiments carried out in a commercial ultrahigh vacuum system, equipped with a hemispherical electron energy analyser (SPECS LH-10, Berlin, Germany) and a twin anode X-ray gun for XPS measurements. The base pressure was 5 × 10⁻¹⁰ mbar. Unmonochromatized Al K_α line at 1486.6 eV and an analyser pass energy of

97 eV were used in all XPS measurements. The binding energies were calculated with reference to the energy of C 1 s peak of contaminant carbon at 285 eV and the highest binding energy peak for Ce⁴⁺ d_{3/2} at 916.5 eV. The surface composition of all samples in terms of atomic ratios was calculated, using a Shirley-type background and empirical cross section factors for XPS.

The platinum content of all the catalysts was determined by an X-ray Fluorescence (XRF) spectrometer (Canberra 1510, Mirion Technologies, München, Germany) equipped with Si/Li detector at 22 keV. The powders were mixed with silica, while tellurium oxide was used as reference.

The morphology of the nanostructured carriers and catalysts was observed by scanning electron microscopy (SEM, LEO SUPRA 35 VP (Carl Zeiss SMT AG Company, Oberkochen, Germany)), and transmission electron microscopy (TEM, FEI Titan G² 60–300, FEI, Gräfelfing, Germany), equipped with a field emission gun (FEG), a monochromator, three condenser lenses system, an objective lens system, image correction (Cs-corrector), HAADF (High-Angle Annular Dark-Field) detector (FEI, Gräfelfing, Germany) and EDS (Energy Dispersive X-ray Spectroscopy) spectrometer (FEI, Gräfelfing, Germany) with a Si (Li) detector and maximum of 20,000 cps. Particle size distribution was obtained by measuring diameter of at least 200 particles in different areas of the catalyst. Phase identification was performed by using the FFT generated from high-resolution TEM images. The elements mapping was carried out in the STEM mode by collecting point by point EDS spectrum of each of the corresponding pixel in the map.

3.4. Catalysts Evaluation in Steam Reforming of Methanol

The catalytic performance for the steam reforming of methanol (SRM) was studied in a laboratory flow system with a fixed-bed reactor, at atmospheric pressure, in the temperature range of 190–220 °C, previously described [27]. The catalyst weight was 0.3 g and the total flow rate of the reaction mixture (5 vol.% CH₃OH/7.5 vol.% H₂O/He) was 70 cm³ min⁻¹ (W/F = 0.257 g·s·cm⁻³). Product and reactant analysis were carried out by an Agilent Technologies (Waldbronn, Germany), 6820 GC System, equipped with TCD (Thermal Conductivity Detector) and FID (Flame Ionization Detector). Catalytic activity was evaluated in terms of methanol conversion and reaction rate either per g of catalyst or per g of loaded platinum. Selectivity to the carbon-containing product was determined based on carbon mol: $S_i = n_i C_i / \sum n_i C_i$, where n_i is the number of carbon atoms in product i and C_i is the concentration of carbon-containing product i . The selectivity of H₂ was calculated as follows:

$$\text{Hydrogen selectivity (\%)} = \frac{3C_{\text{CO}_2} + 2C_{\text{CO}} - C_{\text{CH}_4} + 2C_{\text{HCOOCH}_3} + C_{\text{HCHO}} + 2C_{\text{HCOOH}}}{3(C_{\text{CO}_2} + C_{\text{CO}} + C_{\text{CH}_4}) + 6C_{\text{HCOOCH}_3} + 3C_{\text{HCHO}} + 3C_{\text{HCOOH}}} \times 100 \quad (2)$$

4. Conclusions

Highly active and selective nanostructured catalysts for the steam reforming of methanol at low temperatures ($T < 220$ °C), were prepared via the impregnation and deposition-precipitation methods. Various amounts of platinum were uniformly and finely dispersed onto the surface of hydrothermally synthesized titania nanotubes and ceria nanorods, as confirmed via HRTEM and S/TEM analysis. Significant enrichment of the CNRs surface was obtained in the case of the (DP) method, more intent in the sample with low loading of platinum, which also contained the highest percentage of active metallic species. Ultra-fine dispersion of platinum species with size of less than 1 nm in the case of 0.3 wt.% Pt/CNRs catalyst, strongly interacting with surface defects of similar size, in agreement with the STEM, HR-TEM, XRD and Raman analysis, resulted in a highly efficient catalyst for steam reforming of methanol reaction, targeting the operation level of high temperature PEM fuel cells.

Supplementary Materials: The following are available online at <http://www.mdpi.com/2073-4344/8/11/544/s1>, Figure S1: EDX mapping on the reduced 2.35 wt.% Pt/TNTs (DP), Figure S2: EDX mapping on the reduced 3 wt.% Pt/TNTs (I), Figure S3: EDX mapping on the reduced 3 wt.% Pt/CNRs (I), Figure S4: EDX mapping on the reduced 2.45 wt.% Pt/CNRs (DP), Figure S5: N₂ Adsorption/desorption isotherms and pore size distribution (BJH isotherms) for TNTs, Figure S6: N₂ Adsorption/desorption isotherms and pore size distribution (BJH isotherms) for CNRs, Figure S7: N₂ Adsorption/desorption isotherms (top) and pore size distribution (BJH isotherms)

(bottom) for Pt/TNTs (I) (a), (c) and Pt/TNTs (DP) (b), (d), Figure S8: N₂ Adsorption/desorption isotherms (left) and pore size distribution (BJH isotherms) (right) for 3 wt.% Pt/CNRs (I) (a), (b), 2.45 wt.% Pt/CNRs (DP) (c), (d) and 0.3 wt.% Pt/CNRs (DP) (e), (f).

Author Contributions: Conceptualization, G.A. and S.N.; investigation and formal analysis, J.P.; investigation, A.P. and G.S.; writing—original draft preparation, J.P.; writing—review and editing, G.A.

Funding: This research received no external funding.

Acknowledgments: Financial support from The Fuel Cells and Hydrogen Joint Undertaking (FCH-JU-2012-1; Grant agreement No. 325358) is gratefully acknowledged.

Conflicts of Interest: The authors declare no conflict of interest.

References

1. Avgouropoulos, G.; Ioannides, T.; Kallitsis, J.K.; Neophytides, S. Development of an internal reforming alcohol fuel cell: Concept, challenges and opportunities. *Chem. Eng. J.* **2011**, *176–177*, 95–101. [[CrossRef](#)]
2. Avgouropoulos, G.; Schlicker, S.; Schelhaas, K.-P.; Papavasiliou, J.; Papadimitriou, K.D.; Theodorakopoulou, E.; Gourdoupi, N.; Machocki, A.; Ioannides, T.; Kallitsis, J.K.; et al. Performance evaluation of a proof-of-concept 70W internal reforming methanol fuel cell system. *J. Power Sources* **2016**, *307*, 875–882. [[CrossRef](#)]
3. Avgouropoulos, G.; Papavasiliou, J.; Daletou, M.K.; Kallitsis, J.K.; Ioannides, T.; Neophytides, S. Reforming methanol to electricity in a high temperature PEM fuel cell. *Appl. Catal. B* **2009**, *90*, 628–632. [[CrossRef](#)]
4. Avgouropoulos, G.; Papavasiliou, J.; Ioannides, T.; Neophytides, S. Insights on the effective incorporation of a foam-based methanol reformer in a high temperature polymer electrolyte membrane fuel cell. *J. Power Sources* **2015**, *296*, 335–343. [[CrossRef](#)]
5. Papavasiliou, J.; Słowik, G.; Avgouropoulos, G. Redox behavior of a copper-based methanol reformer for fuel cell applications. *Energy Technol.* **2018**, *6*, 1332–1341. [[CrossRef](#)]
6. Olah, G.A.; Goepfert, A.; Prakash, G.K.S. *Beyond Oil and Gas: The Methanol Economy*; Wiley VCH: Weinheim, Germany, 2006.
7. Ghenciu, A.F. Review of fuel processing catalysts for hydrogen production in PEM fuel cell systems. *Curr. Opin. Solid State Mater. Sci.* **2002**, *6*, 389–399. [[CrossRef](#)]
8. Xu, X.; Shuai, K.; Xu, B. Review on copper and palladium based catalysts for methanol steam reforming to produce hydrogen. *Catalysts* **2017**, *7*, 183. [[CrossRef](#)]
9. Sá, S.; Silva, H.; Brandão, L.; Sousa, J.M.; Mendes, A. Catalysts for methanol steam reforming—A review. *Appl. Catal. B* **2010**, *99*, 43–57. [[CrossRef](#)]
10. Avgouropoulos, G.; Paxinou, A.; Neophytides, S. In situ hydrogen utilization in an internal reforming methanol fuel cell. *Int. J. Hydrog. Energy* **2014**, *39*, 18103–18108. [[CrossRef](#)]
11. Papavasiliou, J.; Avgouropoulos, G.; Ioannides, T. CuMnOx catalysts for internal reforming methanol fuel cells: Application aspects. *Int. J. Hydrog. Energy* **2012**, *37*, 16739–16747. [[CrossRef](#)]
12. Avgouropoulos, G.; Neophytides, S. Performance of internal reforming methanol fuel cell under various methanol/water concentrations. *J. Appl. Electrochem.* **2012**, *42*, 719–726. [[CrossRef](#)]
13. Ribeirinha, P.; Mateos-Pedrero, C.; Boaventura, M.; Sousa, J.; Mendes, A. CuO/ZnO/Ga₂O₃ catalyst for low temperature MSR reaction: Synthesis, characterization and kinetic model. *Appl. Catal. B* **2018**, *221*, 371–379. [[CrossRef](#)]
14. Peppley, B.A.; Amphlett, J.C.; Kearns, L.M.; Mann, R.F. Methanol–steam reforming on Cu/ZnO/Al₂O₃. Part 1: The reaction network. *Appl. Catal. A* **1999**, *179*, 21–29. [[CrossRef](#)]
15. Frank, B.; Jentoft, F.C.; Soerijanto, H.; Kröhnert, J.; Schlögl, R.; Schomäcker, R. Steam reforming of methanol over copper-containing catalysts: Influence of support material on microkinetics. *J. Catal.* **2007**, *246*, 177–192. [[CrossRef](#)]
16. Purnama, H.; Ressler, T.; Jentoft, R.E.; Soerijanto, H.; Schlögl, R.; Schomäcker, R. CO formation/selectivity for steam reforming of methanol with a commercial CuO/ZnO/Al₂O₃ catalyst. *Appl. Catal. A* **2004**, *259*, 83–94. [[CrossRef](#)]
17. Talkhoncheh, S.K.; Haghghi, M.; Minaei, S.; Ajamein, H.; Abdollahifar, M. Synthesis of CuO/ZnO/Al₂O₃/ZrO₂/CeO₂ nanocatalysts via homogeneous precipitation and combustion methods used in methanol steam reforming for fuel cell grade hydrogen production. *RSC Adv.* **2016**, *6*, 57199–57209. [[CrossRef](#)]

18. Park, J.E.; Yim, S.-D.; Kim, C.S.; Park, E.D. Steam reforming of methanol over Cu/ZnO/ZrO₂/Al₂O₃ catalyst. *Int. J. Hydrog. Energy* **2014**, *39*, 11517–11527. [[CrossRef](#)]
19. Tong, W.; West, A.; Cheung, K.; Yu, K.-M.; Tsang, S.C.E. Dramatic effects of gallium promotion on methanol steam reforming Cu–ZnO Catalyst for hydrogen production: Formation of 5 Å copper clusters from Cu–ZnGaO_x. *ACS Catal.* **2013**, *3*, 1231–1244. [[CrossRef](#)]
20. Yu, K.M.K.; Tong, W.; West, A.; Cheung, K.; Li, T.; Smith, G.; Guo, Y.; Tsang, S.C.E. Non-syngas direct steam reforming of methanol to hydrogen and carbon dioxide at low temperature. *Nat. Commun.* **2012**, *3*, 1230. [[CrossRef](#)] [[PubMed](#)]
21. Agrell, J.; Birgersson, H.; Boutonnet, M.; Melian-Cabrera, I.; Navarro, R.M.; Fierro, J.L.G. Production of hydrogen from methanol over Cu/ZnO catalysts promoted by ZrO₂ and Al₂O₃. *J. Catal.* **2003**, *219*, 389–403. [[CrossRef](#)]
22. Lindstrom, B.; Pettersson, L.J.; Menon, P.G. Activity and characterization of Cu/Zn, Cu/Cr and Cu/Zr on γ -alumina for methanol reforming for fuel cell vehicles. *Appl. Catal. A* **2002**, *234*, 111–125. [[CrossRef](#)]
23. Rameshan, C.; Stadlmayr, W.; Penner, S.; Lorenz, M.H.; Memmel, N.; Hävecker, M.; Blume, R.; Teschner, D.; Rocha, T.; Zemlyanov, D.; et al. Hydrogen production by methanol steam reforming on copper boosted by zinc-assisted water activation. *Angew. Chem. Int. Ed.* **2012**, *51*, 3002–3006. [[CrossRef](#)] [[PubMed](#)]
24. Mrad, M.; Gennequin, C.; Aboukaïs, A.; Abi-Aad, E. Cu/Zn-based catalysts for H₂ production via steam reforming of methanol. *Catal. Today* **2011**, *176*, 88–92. [[CrossRef](#)]
25. Tsai, M.-C.; Wang, J.-H.; Shen, C.-C.; Yeh, C.-T. Promotion of a copper–zinc catalyst with rare earth for the steam reforming of methanol at low temperatures. *J. Catal.* **2011**, *279*, 241–245. [[CrossRef](#)]
26. Yong, S.T.; Ooi, C.W.; Chai, S.P.; Wu, X.S. Review of methanol reforming-Cu-based catalysts, surface reaction mechanisms, and reaction schemes. *Int. J. Hydrog. Energy* **2013**, *38*, 9541–9552. [[CrossRef](#)]
27. Papavasiliou, J.; Avgouropoulos, G.; Ioannides, T. Combined steam reforming of methanol over Cu–Mn spinel oxide catalysts. *J. Catal.* **2007**, *251*, 7–20. [[CrossRef](#)]
28. Huang, G.; Liaw, B.-J.; Jhang, C.-J.; Chen, Y.-Z. Steam reforming of methanol over CuO/ZnO/CeO₂/ZrO₂/Al₂O₃ catalysts. *Appl. Catal. A* **2009**, *358*, 7–12. [[CrossRef](#)]
29. Jones, S.D.; Neal, L.M.; Hagelin-Weaver, H.E. Steam reforming of methanol using Cu–ZnO catalysts supported on nanoparticle alumina. *Appl. Catal. B* **2008**, *84*, 631–642. [[CrossRef](#)]
30. Papavasiliou, J.; Avgouropoulos, G.; Ioannides, T. Production of hydrogen via combined steam reforming of methanol over CuO–CeO₂ catalysts. *Catal. Commun.* **2004**, *5*, 231–235. [[CrossRef](#)]
31. Chang, C.-C.; Hsu, C.-C.; Chang, C.-T.; Chen, Y.-P.; Liaw, B.-J.; Chen, Y.Z. Effect of noble metal on oxidative steam reforming of methanol over CuO/ZnO/Al₂O₃ catalyst. *Int. J. Hydrog. Energy* **2012**, *37*, 11176–11184. [[CrossRef](#)]
32. Rameshan, C.; Lorenz, H.; Armbrüster, M.; Kasatkin, I.; Klötzer, B.; Götsch, T.; Ploner, K.; Penner, S. Impregnated and co-precipitated Pd–Ga₂O₃, Pd–In₂O₃ and Pd–Ga₂O₃–In₂O₃ catalysts: Influence of the microstructure on the CO₂ selectivity in methanol steam reforming. *Catal. Lett.* **2018**, *148*, 3062–3071. [[CrossRef](#)] [[PubMed](#)]
33. Martinelli, M.; Jacobs, G.; Graham, U.M.; Davis, B.H. Methanol steam reforming: Na doping of Pt/YSZ provides fine tuning of selectivity. *Catalysts* **2017**, *7*, 148. [[CrossRef](#)]
34. Avgouropoulos, G.; Papavasiliou, J.; Ioannides, T. Hydrogen production from methanol over combustion-synthesized noble metal/ceria catalysts. *Chem. Eng. J.* **2009**, *154*, 274–280. [[CrossRef](#)]
35. Barrios, C.E.; Bosco, M.V.; Baltanás, M.A.; Bonivardi, A.L. Hydrogen production by methanol steam reforming: Catalytic performance of supported-Pd on zinc–cerium oxides' nanocomposites. *Appl. Catal. B* **2015**, *179*, 262–275. [[CrossRef](#)]
36. Matsumura, Y. Enhancement in activity of Pd–Zn catalyst for methanol steam reforming by coprecipitation on zirconia support. *Appl. Catal. A* **2013**, *468*, 350–358. [[CrossRef](#)]
37. Avgouropoulos, G. Isotopic transient study of methanol decomposition over noble metal/ceria catalysts. *Catal. Commun.* **2009**, *10*, 682–686. [[CrossRef](#)]
38. Barrios, C.E.; Baltanás, M.A.; Bosco, M.V.; Bonivardi, A.L. On the surface nature of bimetallic PdZn particles supported on a ZnO–CeO₂ nanocomposite for the methanol steam reforming reaction. *Catal. Lett.* **2018**, *148*, 2233–2246. [[CrossRef](#)]
39. Zhang, Q.; Farrauto, R.J. A PdZn catalyst supported on stabilized ceria for stoichiometric methanol steam reforming and hydrogen production. *Appl. Catal. A* **2011**, *395*, 64–70. [[CrossRef](#)]

40. Armbrüster, M.; Behrens, M.; Föttinger, K.; Friendrich, M.; Gaudry, E.; Matam, S.K.; Sharam, H.R. The intermetallic compound ZnPd and its role in methanol steam reforming. *Catal. Rev. Sci. Eng.* **2013**, *55*, 289–367. [[CrossRef](#)]
41. Lin, L.; Zhou, W.; Gao, R.; Yao, S.; Zhang, X.; Xu, W.; Zheng, S.; Jiang, Z.; Yu, Q.; Li, Y.-W.; et al. Low-temperature hydrogen production from water and methanol using Pt/ α -MoC catalysts. *Nature* **2017**, *544*, 80–83. [[CrossRef](#)] [[PubMed](#)]
42. Suwa, Y.; Ito, S.; Kameoka, S.; Tomishige, K.; Kunimori, K. Comparative study between Zn–Pd/C and Pd/ZnO catalysts for steam reforming of methano. *Appl. Catal. A* **2004**, *267*, 9–16. [[CrossRef](#)]
43. Gomez-Sainero, L.M.; Baker, R.T.; Metcalfe, I.S.; Sahibzada, M.; Concepcion, P.; Lopez-Nieto, J.M. Investigation of Sm₂O₃–CeO₂-supported palladium catalysts for the reforming of methanol: The role of the support. *Appl. Catal. A* **2005**, *294*, 177–187. [[CrossRef](#)]
44. Liu, X.; Men, Y.; Wang, J.; He, R.; Wang, Y. Remarkable support effect on the reactivity of Pt/In₂O₃/MO_x catalysts for methanol steam reforming. *J. Power Sources* **2017**, *364*, 341–350. [[CrossRef](#)]
45. Iwasa, N.; Mayanagi, T.; Nomura, W.; Arai, M.; Takezawa, N. Effect of Zn addition to supported Pd catalysts in the steam reforming of methanol. *Appl. Catal. A* **2003**, *248*, 153–160. [[CrossRef](#)]
46. Chin, Y.H.; Dagle, R.; Hu, J.L.; Dohnalkova, A.C.; Wang, Y. Steam reforming of methanol over highly active Pd/ZnO catalyst. *Catal. Today* **2002**, *77*, 79–88. [[CrossRef](#)]
47. Tahay, P.; Khani, Y.; Jabari, M.; Bahadoran, F.; Safari, N. Highly porous monolith/TiO₂ supported Cu, Cu-Ni, Ru, and Pt catalysts in methanol steam reforming process for H₂ generation. *Appl. Catal. A* **2018**, *554*, 44–53. [[CrossRef](#)]
48. Flytzani-Stephanopoulos, M. Gold atoms stabilized on various supports catalyze the water-gas shift reaction. *Acc. Chem. Res.* **2014**, *47*, 783–792. [[CrossRef](#)] [[PubMed](#)]
49. Li, G.; Jin, R. Atomically precise gold nanoclusters as new model catalysts. *Acc. Chem. Res.* **2013**, *46*, 1749–1758. [[CrossRef](#)] [[PubMed](#)]
50. Pyykkö, P. Magic nanoclusters of gold. *Nat. Nanotechnol.* **2007**, *2*, 273–274. [[CrossRef](#)] [[PubMed](#)]
51. Lykaki, M.; Pachatouridou, E.; Carabineiro, S.A.C.; Iliopoulou, E.; Andriopoulou, C.; Kallithrakas-Kontos, D.; Boghosian, S.; Konsolakis, M. Ceria nanoparticles shape effects on the structural defects and surface chemistry: Implications in CO oxidation by Cu/CeO₂ catalysts. *Appl. Catal. B* **2018**, *230*, 18–28. [[CrossRef](#)]
52. Tinoco, M.; Fernandez-Garcia, S.; Lopez-Haro, M.; Hungria, A.B.; Chen, X.; Blanco, G.; Perez-Omil, J.A.; Collins, S.E.; Okuno, H.; Calvino, J.J. Critical influence of nanofaceting on the preparation and performance of supported gold catalysts. *ACS Catal.* **2015**, *5*, 3504–3513. [[CrossRef](#)]
53. Chen, S.; Li, L.; Hu, W.; Huang, X.; Li, Q.; Xu, Y.; Zuo, Y.; Li, G. Anchoring high-concentration oxygen vacancies at interfaces of CeO_{2-x}/Cu toward enhanced activity for preferential CO oxidation. *ACS Appl. Mater. Interfaces* **2015**, *7*, 22999–23007. [[CrossRef](#)] [[PubMed](#)]
54. Ge, M.; Cai, J.; Iocozzia, J.; Cao, C.; Huang, J.; Zhang, X.; Shen, J.; Wang, S.; Zhang, S.; Zhang, K.-Q.; et al. A review of TiO₂ nanostructured catalysts for sustainable H₂ generation. *Int. J. Hydrog. Energy* **2017**, *42*, 8418–8449. [[CrossRef](#)]
55. Zhang, Y.; Jiang, Z.; Huang, J.; Lim, L.Y.; Li, W.; Deng, J.; Gong, D.; Tang, Y.; Lai, Y.; Chen, Z. Titanate and titania nanostructured materials for environmental and energy applications: A review. *RSC Adv.* **2015**, *5*, 79479–79510. [[CrossRef](#)]
56. Avgouropoulos, G.; Ioannides, T. Effect of synthesis parameters on catalytic properties of CuO–CeO₂. *Appl. Catal. B* **2006**, *67*, 1–11. [[CrossRef](#)]
57. Papavasiliou, J.; Rawski, M.; Vakros, J.; Avgouropoulos, G. A novel post-synthesis modification of CuO–CeO₂ catalysts: Effect on their activity for selective CO oxidation. *ChemCatChem* **2018**, *10*, 2096–2106. [[CrossRef](#)]
58. Zhuang, Z.K.; Yang, Z.M.; Zhou, S.Y.; Wang, H.Q.; Sun, C.L.; Wu, Z.B. Synergistic photocatalytic oxidation and adsorption of elemental mercury by carbon modified titanium dioxide nanotubes under visible light LED irradiation. *Chem. Eng. J.* **2014**, *253*, 16–23. [[CrossRef](#)]
59. Vijayan, B.K.; Dimitrijevic, N.M.; Wu, J.; Gray, K.A. The effects of Pt doping on the structure and visible light photoactivity of titania nanotubes. *J. Phys. Chem. C* **2010**, *114*, 21262–21269. [[CrossRef](#)]
60. Baiju, K.V.; Shukla, S.; Biju, S.; Reddy, M.L.P.; Warriar, K.G.K. Morphology-dependent dye-removal mechanism as observed for Anatase—Titania photocatalyst. *Catal. Lett.* **2009**, *131*, 663–671. [[CrossRef](#)]

61. Agarwal, S.; Lefferts, L.; Mojet, B.L.; Ligthart, D.A.J.M.; Hensen, E.J.M.; Mitchell, D.R.G.; Erasmus, W.J.; Anderson, B.G.; Olivier, E.J.; Neethling, J.H.; et al. Exposed surfaces on the shape-controlled ceria nanoparticles revealed through AC-TEM and water-gas shift reactivity. *Chem. Sustain. Chem.* **2013**, *6*, 1898–1906. [[CrossRef](#)] [[PubMed](#)]
62. Peng, R.; Li, S.; Ren, Q.; Chen, L.; Fu, M.; Wu, J.; Ye, D. Size effect of Pt nanoparticles on the catalytic oxidation of toluene over Pt/CeO₂ catalysts. *Appl. Catal. B* **2018**, *220*, 462–470. [[CrossRef](#)]
63. Peng, R.; Sun, X.; Li, S.; Chen, L.; Fu, M.; Wu, J.; Ye, D. Shape effect of Pt/CeO₂ catalysts on the catalytic oxidation of toluene. *Chem. Eng. J.* **2016**, *306*, 1234–1243. [[CrossRef](#)]
64. Si, R.; Flytzani-Stephanopoulos, M. Shape and Crystal-plane effects of nanoscale ceria on the activity of Au-CeO₂ catalysts for the water-gas shift reaction. *Angew. Chem. Int. Ed.* **2008**, *47*, 2884–2887. [[CrossRef](#)] [[PubMed](#)]
65. Florea, I.; Feral-Martin, C.; Majimel, J.; Ihiawakrim, D.; Hirlimann, C.; Ersen, O. Three-Dimensional tomographic Analyses of CeO₂ nanoparticles. *Cryst. Growth Des.* **2013**, *13*, 1110–1121. [[CrossRef](#)]
66. Tao, L.; Shi, Y.; Huang, Y.-C.; Chen, R.; Zhang, Y.; Huo, J.; Zou, Y.; Yu, G.; Dong, C.-L.; Wang, S. Interface engineering of Pt and CeO₂ nanorods with unique interaction for methanol oxidation. *Nano Energy* **2018**, *53*, 604–612. [[CrossRef](#)]
67. Stelmachowski, P.; Ciura, K.; Indyka, P.; Kotarba, A. Facile synthesis of ordered CeO₂ nanorod assemblies: Morphology and reactivity. *Mater. Chem. Phys.* **2017**, *201*, 139–146. [[CrossRef](#)]
68. He, H.; Yang, P.; Li, J.; Shi, R.; Chen, L.; Zhang, A.; Zhu, Y. Controllable synthesis, characterization, and CO oxidation activity of CeO₂ nanostructures with various morphologies. *Ceram. Int.* **2016**, *42*, 7810–7818. [[CrossRef](#)]
69. Mai, H.-X.; Sun, L.-D.; Zhang, Y.-W.; Si, R.; Feng, W.; Zhang, H.-P.; Liu, H.-C.; Yan, C.-H. Shape selective synthesis and oxygen storage behavior of Ceria nanopolyhedra, nanorods, and nanocubes. *J. Phys. Chem. B* **2005**, *109*, 24380–24385. [[CrossRef](#)] [[PubMed](#)]
70. Tong, T.; Liu, X.; Guo, Y.; Banis, M.N.; Hu, Y.; Wang, Y. The critical role of CeO₂ crystal-plane in controlling Pt chemical states on the hydrogenolysis of furfuryl alcohol to 1,2-Pentanediol. *J. Catal.* **2018**, *365*, 420–428. [[CrossRef](#)]
71. Abida, B.; Chirchi, L.; Baranton, S.; Napporn, T.W.; Kochkar, H.; Léger, J.-M.; Ghorbel, A. Preparation and characterization of Pt/TiO₂ nanotubes catalyst for methanol electro-oxidation. *Appl. Catal. B* **2011**, *106*, 609–615. [[CrossRef](#)]
72. Yi, N.; Si, R.; Saltsburg, H.; Flytzani-Stephanopoulos, M. Steam reforming of methanol over ceria and gold-ceria nanoshapes. *Appl. Catal. B* **2010**, *95*, 87–92. [[CrossRef](#)]
73. Baiju, K.V.; Shukla, S.; Biju, S.; Reddy, M.L.P.; Warriar, K.G.K. Hydrothermal processing of dye-adsorbing one-dimensional hydrogen titanate. *Mater. Lett.* **2009**, *63*, 923–926. [[CrossRef](#)]
74. Toledo-Antonio, J.A.; Ángeles-Chávez, C.; Cortés-Jácome, M.A.; Cuauhtémoc-López, I.; López-Salinas, E.; Pérez-Luna, M.; Ferrat-Torres, G. Highly dispersed Pt-Ir nanoparticles on titania nanotubes. *Appl. Catal. A* **2012**, *437*, 155–165. [[CrossRef](#)]
75. Kim, S.-J.; Yun, Y.-U.; Oh, H.-J.; Hong, S.H.; Roberts, C.A.; Routray, K.; Wachs, I.E. Characterization of hydrothermally prepared titanate nanotube powders by ambient and in situ Raman spectroscopy. *J. Phys. Chem. Lett.* **2010**, *1*, 130–135. [[CrossRef](#)]
76. Gao, Y.; Wang, W.; Chang, S.; Huang, W. Morphology effect of CeO₂ support in the preparation, metal-support interaction, and catalytic performance of Pt/CeO₂ catalysts. *ChemCatChem* **2013**, *5*, 3610–3620. [[CrossRef](#)]
77. Pushkarev, V.V.; Kovalchuk, V.I.; d'Itri, J.L. Probing defect sites on the CeO₂ surface with dioxygen. *J. Phys. Chem. B* **2004**, *108*, 5341–5348. [[CrossRef](#)]
78. Daniel, M.; Loridant, S. Probing reoxidation sites by in situ Raman spectroscopy: Differences between reduced CeO₂ and Pt/CeO₂. *J. Raman Spectrosc.* **2012**, *43*, 1312–1319. [[CrossRef](#)]
79. Rui, Z.; Chen, L.; Chen, H.; Ji, H. Strong metal-support interaction in Pt/TiO₂ induced by mild HCHO and NaBH₄ solution reduction and its effect on catalytic toluene combustion. *Ind. Eng. Chem. Res.* **2014**, *53*, 15879–15888. [[CrossRef](#)]
80. Chen, H.; Tang, M.; Rui, Z.; Wang, X.; Ji, H. ZnO modified TiO₂ nanotube array supported Pt catalyst for HCHO removal under mild conditions. *Catal. Today* **2016**, *264*, 23–30. [[CrossRef](#)]

81. Wang, X.; Yuan, X.; Liu, X.; Dong, W.; Dong, C.; Lou, M.; Li, J.; Lin, T.; Huang, F. Monodisperse Pt nanoparticles anchored on N-doped black TiO₂ as high performance bifunctional electrocatalyst. *J. Alloys Compd.* **2017**, *701*, 669–675. [[CrossRef](#)]
82. Su, Y.; Deng, Y. Effect of structure on the photocatalytic activity of Pt-doped TiO₂ nanotubes. *Appl. Surf. Sci.* **2011**, *257*, 9791–9795. [[CrossRef](#)]
83. Geormezi, M.; Paloukis, F.; Orfanidi, A.; Shroti, N.; Daletou, M.; Neophytides, S.G. The structure and stability of the anodic electrochemical interface in a high temperature polymer electrolyte membrane fuel cell under reformat feed. *J. Power Sources* **2015**, *285*, 499–509. [[CrossRef](#)]
84. Orfanidi, A.; Daletou, M.; Neophytides, S.G. Mitigation strategy towards stabilizing the electrochemical interface under high CO and H₂O containing reformat gas feed. *Electrochim. Acta* **2017**, *233*, 218–228. [[CrossRef](#)]
85. Araya, S.S.; Grigoras, I.F.; Zhou, F.; Andreasen, S.J.; Kaer, S.K. Performance and endurance of a high temperature PEM fuel cell operated on methanol reformat. *Int. J. Hydrog. Energy* **2014**, *39*, 18343–18350. [[CrossRef](#)]



© 2018 by the authors. Licensee MDPI, Basel, Switzerland. This article is an open access article distributed under the terms and conditions of the Creative Commons Attribution (CC BY) license (<http://creativecommons.org/licenses/by/4.0/>).